A.K. Sugihara El Maghraby, A. Grubisic, C. Colombo, A. Tatnall
A Novel Interferometric Microwave Radiometer Concept Using Satellite Formation Flight for Geostationary Atmospheric Sounding
IEEE Transactions on Geoscience and Remote Sensing, Vol. 56, N. 6, 2018, p. 3487-3498
doi:10.1109/TGRS.2018.2800534

The final publication is available at https://doi.org/10.1109/TGRS.2018.2800534

A Novel Interferometric Microwave Radiometer Concept Using Satellite Formation Flight for Geostationary Atmospheric Sounding

Ahmed Kiyoshi Sugihara El Maghraby, Angelo Grubišić, Camilla Colombo, and Adrian Tatnall

***Abstract*— For most Earth observation applications, passive microwave radiometry from the geostationary orbit requires prohibitively large apertures for conventional single-satellite platforms. This paper proposes a novel interferometric technique capable of synthesizing these apertures using satellite formation flight. The significance of such concept is in its capacity to synthesize microwave apertures of conceptually unconstrained size in space for the first time. The technique is implemented in two formation flight configurations: a formation of a single full-sized satellite with microsatellites and a formation of several full-sized satellites. Practical advantages and challenges of these configurations are explored by applying them to geostationary atmospheric sounding at 53 GHz, the lowest sounding frequency considered for future sounder concepts Geostationary Atmospheric Sounder, GeoSTAR, and Geostationary Interferometric Microwave Sounder. The two configurations produce apertures of 14.4 and 28.8 m, respectively, and a spatial resolution of 16.7 and 8.3 km, respectively, from the geostationary orbit. The performance of these interferometers is simulated, and the challenges identified are threefold. First, intersatellite ranging in micrometer-level precision is required. Second, the extremely sparse design suggests that further innovation is necessary to improve radiometric resolution. Third, the presence of long baselines suggests extreme decorrelation effects are expected. While the first requirement has already been demonstrated on ground, the other two remain for future research. This technique can be implemented at arbitrary microwave frequencies and arbitrary circular orbits, meaning it can also be applied to other geostationary applications, or to achieve unprecedented spatial resolution from lower orbits, or to extend the accessible frequencies into lower frequency radio waves.**

***Index Terms*— Atmospheric sounding, microwave radiometry, mission concept, satellite formation flight, synthetic aperture imaging.**

I. Introduction

PASSIVE microwave radiometry is a highly versatile tool for satellite remote sensing of the Earth, producing a wide variety of meteorological and climate data products of both the surface and the atmosphere. Placing the instrument in the geostationary orbit has recently become feasible using interferometric techniques demonstrated by the Microwave Imaging Radiometer using Aperture Synthesis (MIRAS) instrument on board Soil Moisture and Ocean Salinity (SMOS) [1]. Ongoing research focuses on applying the technique to develop a geostationary sounder at higher microwave frequencies for real-time temperature and humidity sounding, in order to significantly improve the accuracy of numerical weather prediction (NWP).

Conventional geostationary weather satellites are equipped with optical and IR sensors, which are unable to provide sounding data under cloudy conditions. Microwave sounders, on the other hand, operate under all weather conditions and have been vital for NWP; however, the achievable spatial resolution is limited at the low Earth orbit, where the current state of the art is 3 h, achieved by the Global Precipitation Measurement constellation [2]. For the significant improvement anticipated in NWP accuracy by introducing global real-time sounding, a full microwave sounding capability from the geostationary orbit is highly desired, and has been in consideration for the past number of years [3].

Due to the diffraction limit, the aperture sizes necessary to achieve the required spatial resolution are prohibitive for conventional real aperture techniques. Current research aims to synthesize these apertures using interferometric techniques, where major developments include radiometer concepts GeoSTAR (NASA, [4]), Geostationary Atmospheric Sounder (GAS) (European Space Agency, [5]), and Geostationary Interferometric Microwave Sounder (GIMS) (National Space Science Center, China, [6]). These instruments, however, are all designed for single-satellite platforms, and the achievable aperture sizes are still fundamentally constrained by satellite's physical size. If larger apertures are required, these may only be synthesized using a fleet of formation flying satellites.

In this paper, we explore the feasibility of a novel interferometric technique, previously described in [7], in which the available interferometric techniques are extended using satellite formation flight to further extend the achievable aperture sizes into such sizes that may not be achieved using single satellites. Two configurations applying this technique are simulated at 53 GHz, the lowest sounding frequency for the geostationary atmospheric sounder concepts, to explore the practical implications of formation flight interferometry.

Manuscript received March 9, 2017; revised October 10, 2017; accepted January 14, 2018. Date of publication March 23, 2018; date of current version May 21, 2018. This work was supported by the U.K. Engineering and Physical Sciences Research Council under Award 1503202. *(Corresponding author: Ahmed Kiyoshi Sugihara El Maghraby.)*

A. K. Sugihara El Maghraby, A. Grubišić, and A. Tatnall are with the Astronautics Research Group, University of Southampton, Southampton SO17 1BJ, U.K. (e-mail: asem1g14@soton.ac.uk; a.grubisic@soton.ac.uk; art4@soton.ac.uk).

C. Colombo is with the Department of Aerospace Science and Technology, Politecnico di Milano, 20133 Milan, Italy (e-mail: camilla.colombo@polimi.it).

Color versions of one or more of the figures in this paper are available online at http://ieeexplore.ieee.org.

Digital Object Identifier 10.1109/TGRS.2018.2800534

The time is appropriate for discussing such a technique, since missions accomplished using satellite formation flight are now growing rapidly, giving rise to new experience and techniques for sustained formation flight. To list a few examples, Gravity Recovery and Climate Experiment (GRACE) [8] and Gravity Recovery and Interior Laboratory (GRAIL) [9] perform gravimetry with GRACE follow-on [10] planned, TerraSAR-X add-on for Digital Elevation Measurement (TanDEM-X) [11] performs bistatic radar, and the Laser Interferometer Space Antenna (LISA) [12] is a planned gravitational wave antenna. The speed at which new precision formation flying technology is being demonstrated on nanosatellite platforms is especially worthy of attention [13]. The synthesis of microwave apertures has been in discussion as a possible application for satellite formation flight, and has been realized for active microwave missions with TanDEM-X. However, formation flight for passive aperture synthesis is still unprecedented, and this is the topic of this paper.

The significance of the proposed concept is in its capacity to synthesize microwave apertures of conceptually unconstrained size in space for the first time. The concept can be implemented at arbitrary microwave frequencies and arbitrary circular orbits for a variety of observables. In addition to geostationary atmospheric sounding, the technique may be applied to achieve unprecedented spatial resolution from lower orbits, or to extend the accessible frequencies into lower frequencies.

Section II introduces and develops the tools necessary to arrive at the suitable formation flight geometries. Section III applies these tools to size suitable constellations for geostationary atmospheric sounding. The simulated imaging performance of the concepts is presented in Section IV. The key result of this paper is the description of performance degradation due to the satellite relative position uncertainty, presented in Section IV-B. Section V then discusses these results.

II. Multisatellite Interferometric Radiometry

The purpose of radiometers is to map the brightness temperature of the observed scene at a specific microwave frequency so that useful meteorological information can be extracted from such maps. The diffraction limit defines the radiometer's angular spatial resolution as proportional to the ratio λ/D—the ratio between the instrument's center wavelength and its aperture size. This indictates that in order to place a radiometer on the geostationary orbit while maintaining the spatial resolution achievable from the low Earth orbit, an aperture approximately 50 times larger is required. The interferometric techniques demonstrated by MIRAS may be directly implemented with a multisatellite architecture to synthesize these apertures.

An interferometer maps the scene brightness using a set of antennas which use a common local oscillator. In the case of multisatellite interferometers, this must be a set of synchronized oscillators that reside in each satellite. The size of the synthesized aperture is determined by the interferometer's maximum baseline—the longest separation distance between the free-flying antennas. The baseline vector is defined between each pair of antennas, and it is the separation vector between the phase centers of these antennas normalized by the wavelength, with components $[u, v, w]$ in the $[x, y, z]$ spatial dimensions with the $+z$-axis pointing toward the target. Baseline vectors between free-flying elements must be continuously measured at high precision. Under these conditions, the signals observed by each pair of antennas are cross-correlated to produce a point-sample measurement of an intermediate quantity called the visibility map, located at the baseline vectors $[u, v, w]$. For a single polarization and a long enough integration time, the visibility measured between antennas 1 and 2 is related to the scene brightness temperature map as [14], [15]

$$V_{1,2}(u,v,w) = \frac{1}{\sqrt{\Omega_1\Omega_2}} \iint_{\xi^2+\eta^2<1} \tilde{T}_B(\xi,\eta) \cdot \tilde{r}\left(-\frac{u\xi+v\eta+w\sqrt{1-\xi^2-\eta^2}}{f_0}\right) \cdot e^{-2\pi i(u\xi+v\eta+w\sqrt{1-\xi^2-\eta^2})} d\xi d\eta \quad (1)$$

for the modified brightness temperature map

$$\tilde{T}_B(\xi,\eta) = \frac{(T_B(\xi,\eta)-T_r)F_{n1}(\xi,\eta)F_{n2}^*(\xi,\eta)}{\sqrt{1-\xi^2-\eta^2}} \quad (2)$$

where $T_B(\xi,\eta)$ is the brightness temperature map at the direction cosines $[\xi,\eta]$, and T_r is the physical temperature of both receivers, the contribution of which can be neglected for the purposes of this paper assuming the antennas are sufficiently separated [14], [16]. $\Omega_{1,2}$ and $F_{n1,2}$ are the beam solid angle and normalized voltage pattern, respectively, and $\tilde{r}$ is the fringe-washing function.

While this expression can be expanded to the full polarimetric formulation by following [15], this paper uses the above simplified expression to explore the key properties of the proposed interferometers. The definition of the modified map is convenient, since with a planar array ($w = 0$) and negligible fringe-washing function ($\tilde{r} = 1$) [17], (1) collapses to a spatial Fourier transform. Hence, the brightness temperature can be retrieved by applying variants of inverse Fourier transform to the measured visibility.

Visibility measured between all possible pairs of antennas produce the visibility sampling pattern of the interferometer. The shape and size of the sampling pattern are closely linked to the shape of the synthesized aperture, and are the key determinants of the imaging performance. A circular aperture provides equal spatial resolution in all directions [18] and this is achieved by mission concepts GAS and GIMS by physically rotating the array [5], [6]. The size of the pattern reflects the size of the synthesized aperture, and consequently the angular resolution. Since the sampling pattern is determined by the geometry of the formation flight, this motivates the search for a suitable set of formation flight geometries.

To explore the effect of formation flight on the visibility sampling pattern, first consider the array geometry and its sampling pattern of the monolithic Y-shaped array as adopted by the MIRAS instrument, shown in Fig. 1. The modification of this pattern by the addition of free-flying antenna elements is now explored. Given the Y-shaped array, we propose two

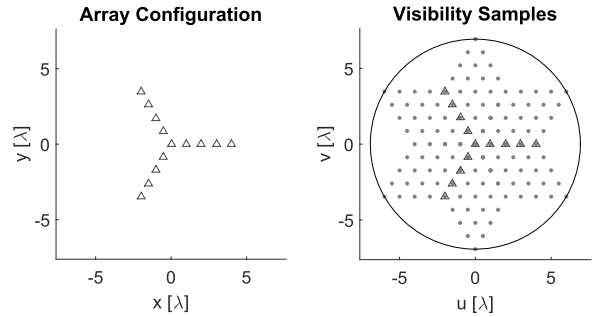

Fig. 1. Array geometry and sampling pattern of a 15-element Y-shaped interferometer. By rotating the array, all visibility within the circular bound can be sampled.

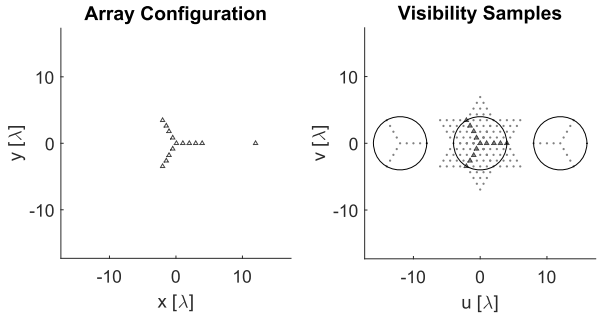

Fig. 2. Effect of introducing a single element to the array, shown in Fig. 1, on the visibility sampling pattern.

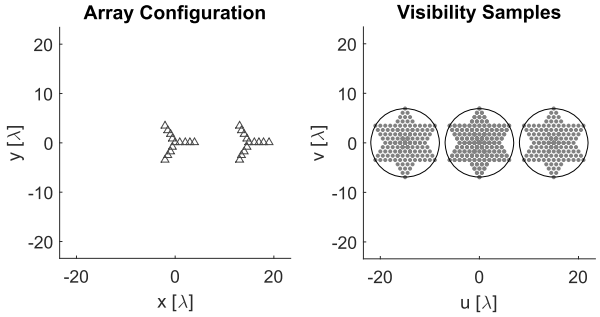

Fig. 3. Effect of introducing a duplicate of the array, shown in Fig. 1, on the visibility sampling pattern.

types of free-flying antennas that may be introduced: the free-flying single antenna and the identical copy of the given array. The effects of these two cases are shown in Figs. 2 and 3, respectively, and are now discussed.

A. Single-Element Companions

Given the distribution of antennas mounted on a single satellite, the addition of a single antenna at any distance away copies the geometry of the original array in the visibility sampling pattern at that distance. This is shown in Fig. 2, where a Y-shaped set of visibility samples is introduced at the location of the single element. The advantage of this configuration is that these single elements may be flown on microsatellites that weigh a few tens of kilograms. Rotating the central array about the z-axis also rotates the geometry of the array in the visibility space about their respective centers, allowing circular visibility samples to be taken.

B. Array Duplication

Given an array of antennas, the introduction of an identical array at any distance copies of visibility sampling pattern of the individual array at the separation distance between the arrays. This is shown in Fig. 3, where the separation of two identical Y-shaped arrays results in copies of the visibility samples separated at the same distance as between the arrays. The advantage to this configuration is its ability to synthesize larger apertures than the Single-Element Companion configuration, at the cost of constellation total mass. As with the first configuration, by rotating both arrays at the same direction and rate, both sampling patterns rotate about their respective centers.

III. Formation Geometries for Geostationary Atmospheric Sounding

The above effects are now applied to find suitable formation configurations that synthesize a single large circular aperture. One scalable configuration is presented for each of the single-element companions and the array duplication effects. The mission is sized with the following considerations in mind. First, 53 GHz is chosen as the radiometer's center frequency since this Oxygen band is employed on GeoSTAR, GAS, and GIMS, allowing direct comparison with these missions. Furthermore, the minimum baseline must be smaller than that specified by the Nyquist sampling criterion to avoid aliasing. This is

$$b_{\min} = \frac{\lambda}{\theta_{\mathrm{AF}}} \tag{3}$$

for alias-free full-width field of view θ_{AF} and wavelength λ. The Earth is 17.4° in diameter from the geostationary orbit, giving the minimum baseline of 3.29λ. A slightly smaller 3λ is chosen for the concepts to include the cold space in the field of view, with a total alias-free field of view of 19.1°. These antennas are distributed along rotating booms. To adhere to currently feasible satellite structures, 4-m booms are chosen, as already operational on the MIRAS instrument. At 53 GHz, a boom of this length can accommodate 236 elements.

A. Single-Element Companion Concept

Applying the mechanism introduced in Section II-A, a set of Single-Element Companions are distributed around a rotating main array in such a way that circular samples, seen in Fig. 2, align in a hexagonal grid to completely fill the visibility space without gaps. The intersatellite separation that allows this is $\sqrt{3}R$, where R is the boom length. At this separation, the hexagonally latticed circular samples touch one another without gaps, synthesizing the largest effective aperture. Larger separation will result in gaps between visibility samples, producing strong sidelobes, and smaller separation will result in redundant visibility overlap, leading to a smaller synthesized aperture. The result is shown in Fig. 4(a), in the nine-companion configuration. Each companion element (labeled A to I) produces a pair of visibility samples with all elements in the central array. The samples shown in Fig. 4(b) shows the visibility sample at one instant. By rotating the central array, each of these Y-shaped samples rotate about their centers, allowing each Y-shaped sample to obtain a circular visibility sample, as shown in Fig. 4(c), labeled with the companion satellite that produces these samples. The overlap

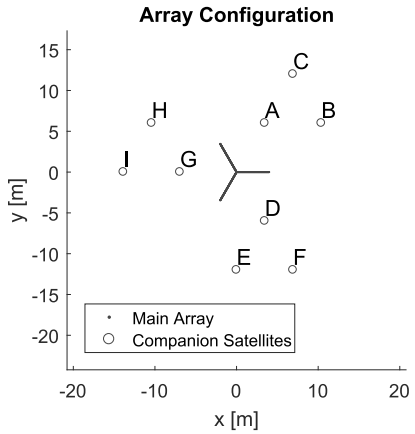

(a)

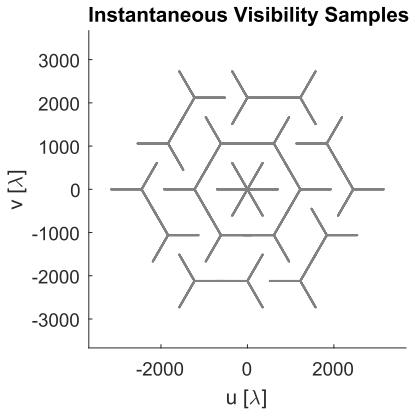

(b)

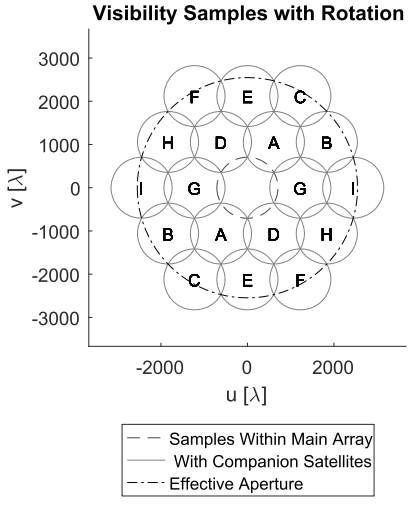

(c)

Fig. 4. Rotating Y-shaped interferometer flies in formation with nine microsatellites, each carrying single antenna elements A to I (a). At a single instant the visibility is sampled in line segments (b). Rotation of the central array leads to a circular effective aperture, the diameter of which is 3.6 times the length of the arms (c). Visibility samples at 53 GHz.

of these circular samples produces the effective aperture, shown in the large circle. Visibility samples outside of this area are ignored to minimize sidelobes.

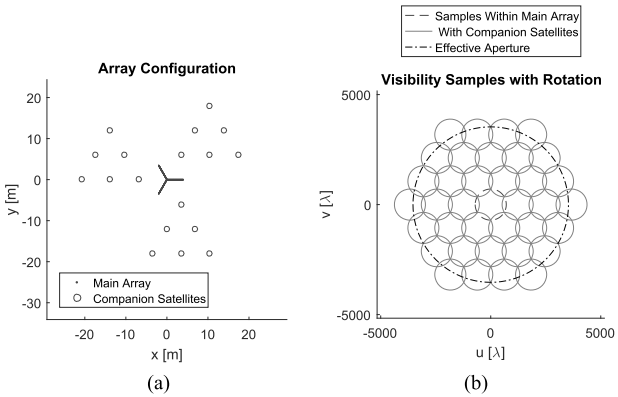

(a) (b)

Fig. 5. Example of an upscaled 18-microsatellite configuration of the Single-Element Companion concept with increased effective aperture diameter of five times the length of the arms. Visibility samples at 53 GHz.

TABLE I
SCALING OF SINGLE-ELEMENT COMPANION CONCEPT

Comps	$\Phi_{\rm eff}$ [m]	S. Res [km]	B. Pairs	$\tau_{\rm tot}$ [min]
3	2.0 R = 8.0	30.1	2,832	69
9	3.6 R = 14.4	16.7	7,080	385
18	5.0 R = 20.0	12.0	13,452	1,856
30	6.5 R = 26.2	9.2	21,948	4,914
45	8.0 R = 32.0	7.5	32,568	8,885
63	9.6 R = 38.2	6.3	45,312	14,207

For number of companion satellites, effective aperture $\Phi_{\rm eff}$, spatial resolution from GEO, total baseline pairs and total integration time for 1 K resolution. Boom length R is 4 m and centre frequency is 53 GHz.

The resulting maximum baseline, which is the effective aperture diameter, is 3.6 times the boom length for the nine-companion option, producing an effective aperture of 14.4 m. This can be scaled larger by employing more companion satellites. Shown in Fig. 5 is an 18-companion variant of the concept with 20.0-m aperture, and larger constellations are listed in Table I. Also shown in the table are the total number of antenna pairs, which will determine the number of complex cross-correlators required per channel.

In the Single-Element Companion concept, only the central samples are redundant, leading to the relatively small number of required correlators. As a result, the sensitivity of this concept suffers, as shown in the last column of Table I, where the total integration time required for 1 K radiometric resolution is listed. This is further discussed in Section V.

B. Array Duplicate Concept

The second concept employs a constellation of six rotating two-boom interferometers flying in a triangular formation. For this particular formation, the two-boom configuration allows for a larger aperture than the Y-shaped arrays. The intersatellite distance in this concept is $2\sqrt{3}R$, which allows the circular visibility samples to overlap when the arrays are rotated, as shown in Fig. 6. Despite the dissimilarity in array configuration, the resultant visibility sampling pattern is identical to the first concept, as shown in Fig. 8. This concept requires that all arrays rotate synchronously and the effective aperture is much larger at 28.8 m compared to the first concept at 14.4 m for the same boom length.

An important difference to the Single-Element Companion concept is the presence of redundant intersatellite baselines,

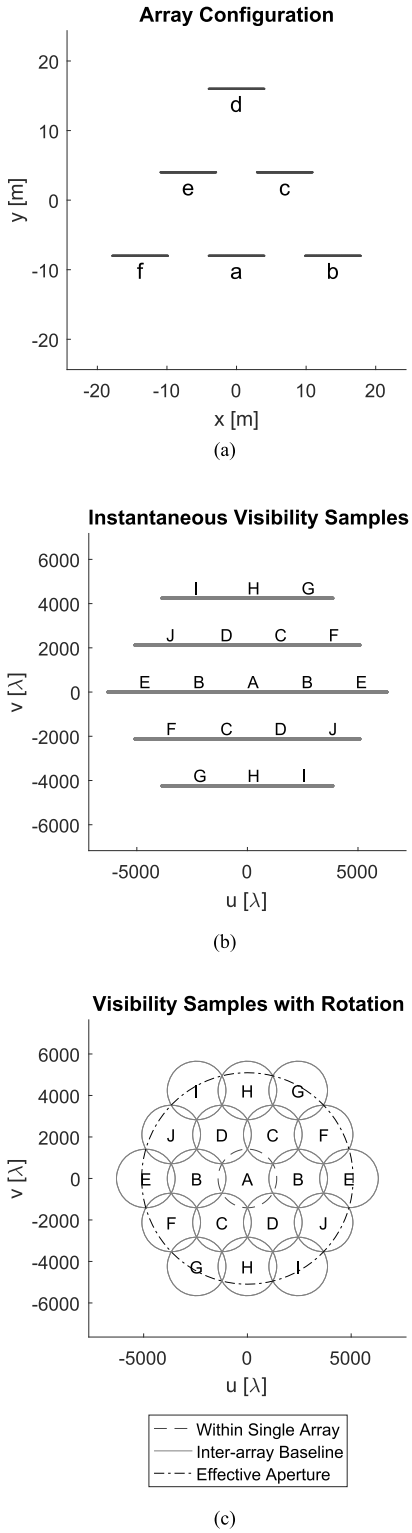

Fig. 6. Six-satellite configuration of the Array Duplicate concept with rotating two-boom interferometers. All booms rotate synchronously to develop a circular aperture with a diameter of 28.8 m with 4-m booms. Visibility samples at 53 GHz.

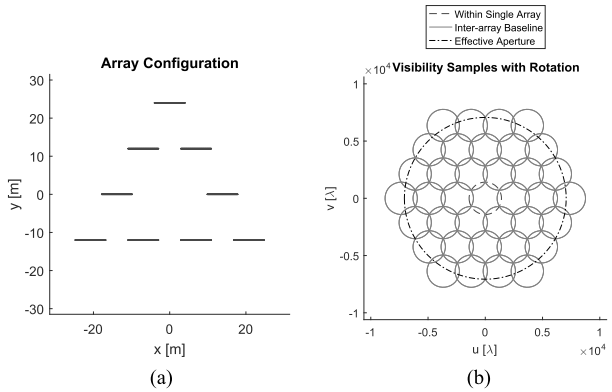

Fig. 7. Upscaled nine-satellite configuration of the Array Duplicate concept with an effective aperture of 40 m with 4-m booms. Visibility samples at 53 GHz.

TABLE II
SCALING OF ARRAY DUPLICATE CONCEPT

Sats	Φ_{eff} [m]	S. Res [km]	B. Pairs	τ_{tot} [min]
3	4.0 R = 16.0	15.0	2,005,056	37
6	7.2 R = 28.8	8.4	8,020,224	77
9	10.0 R = 40.0	6.0	18,045,504	131
12	13.1 R = 52.5	4.6	32,080,896	233
15	16.0 R = 64.0	3.8	50,126,400	363
18	19.1 R = 76.3	3.1	72,182,016	548

For number of satellites. The remaining columns are as defined in Table I.

which is absent in the former configuration. As shown in Fig. 6(c), the instantaneous visibility samples A can now be sampled independently by each individual array, resulting in five redundant measurements. Similarly, visibility samples B are sampled between arrays a and b, arrays f and a, and arrays e and c, resulting in two redundant measurements, and likewise for baselines C and D. Each of E and above has no redundant measurements for the nine-satellite formation. These redundant measurements represent sixfold increase in available signal integration time for A and threefold for B-D, resulting in a significant improvement in radiometric resolution as discussed in Section IV-C. These redundancies also improve the array's tolerance to the uncertainties in the measured baseline vectors, as demonstrated in Section IV-B. The redundant baselines mean that a large number of correlators are needed; however, these can be distributed between all satellites.

The triangular constellation is also scalable for larger effective apertures. Shown in Fig. 7 is the nine-satellite variant of the constellation, and the scaling up to the 18-satellite configuration is summarized in Table II listing effective aperture and achievable spatial resolution, as well as the total number of antenna pairs.

IV. SIMULATING ARRAY PERFORMANCE

To understand the challenges behind the concepts proposed above, their performances are now characterized by means of simulation. The parameters we explore are the arrays' spatial resolution and radiometric resolution, taking into account visibility thermal noise, spatial decorrelation, and baseline error due to the uncertainties in satellite relative position measurement. To find these parameters, the retrieved brightness temperature map is found for a given input map, by simulating the array forward and back. The array is first simulated "forward" to find the measured visibility for an input brightness temperature map by solving (1). The input map

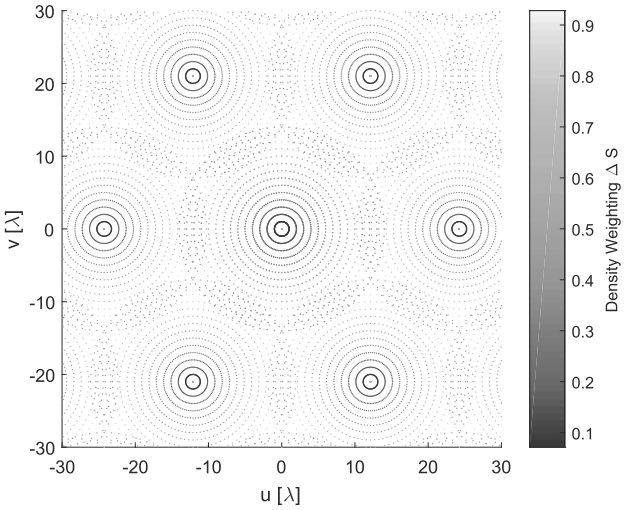

Fig. 8. Visibility sampling pattern obtained by the Single-Element Companion concept and the weighting functions associated with each point sample. These values are calculated by (8). The example uses a small array for clarity: 15 antenna elements per boom separated at 1 λ.

is first replaced by the weighted averaged map $T_B^f(\xi, \eta)$ to account for the decorrelation effects. The formulation for T_B^f is a function of the fringe-washing function, and assuming a rectangular passband the fringe-washing function is a sinc function

$$\tilde{r}(\tau_d) = \text{sinc}(B\tau_d) \tag{4}$$

for predetection bandwidth B and signal delay τ_d. With this, T_B^f can be given as [19]

$$T_B^f(\xi, \eta) = \frac{1}{W}\int_{1-W/2}^{1+W/2} T_B(\sigma\xi, \sigma\eta)d\sigma \tag{5}$$

where $W = B/f_0$ is the relative bandwidth. This is then modified following (2) and applied to (1) where the fringe-washing term can now be removed.

In practice, (1) is executed using fast Fourier transform (FFT). The modified input map is zero-padded and transformed, giving an oversampled visibility map in a rectangular grid. The visibility samples are then taken by interpolating the sampling pattern (Fig. 8) within this map, and the effect of out-of-plane deviation w is approximated as constant phase errors in the individual antennas as performed in [20]. The individual antenna voltage pattern F_n and beamwidth Ω are modeled after the horn antennas applied on the GeoSTAR demonstrator [16] linearly scaled to our 3λ separation such that $\Omega = 0.211$ sr. Circular symmetry is assumed for the beam about its boresight with no pointing errors and all antennas are identical. Receiver bandwidth and noise temperature are also modeled after the GeoSTAR demonstrator.

To simulate the array "backward," the brightness map is retrieved by inverting these visibility measurements. Had the visibility been measured in a regular Cartesian grid, such as rectangular or hexagonal grids, the inverse FFT could have been used [17]. With the proposed rotating arrays, however, the sampling grid is not Cartesian. The proposed sampling pattern is a variant of a polar grid, such that samples are taken at a regular radial and angular intervals—and therefore at regular time intervals. With such strategy, an interlaced polar distribution emerges, as shown in Fig. 8. The visibility samples are then directly inverted with a slower discrete method, following:

$$\hat{T}_B(\xi, \eta) = \frac{\Omega\sqrt{1-\xi^2-\eta^2}}{|F_n|^2} \cdot \sum_{m=1}^{N} V_m W_m \Delta S_m e^{2\pi i(u_m\xi + v_m\eta + w_m\sqrt{1-\xi^2-\eta^2})} \tag{6}$$

where $\hat{T}_B$ is the recovered brightness temperature map for N visibility samples, V_m is the mth visibility sample at its baseline vector $[u_m, v_m, w_m]$. While, in practice, faster algorithms will be needed especially for the larger arrays (e.g., non-uniform fast Fourier transform [21], [22] or pseudo-polar fast Fourier transform [23], [24]), the method is chosen in this paper to avoid errors associated with visibility resampling and gridding. This allows us to isolate the effect of array distortion as an error source in Section IV-B.

W_m is the windowing function applied to reduce the strength of the sidelobes and improve the efficiency of the beam, therefore improving the interferometer's sensitivity. In this case, the Blackman window is used as applied on MIRAS, defined as follows [25]:

$$W_m = 0.42 + 0.5\cos(\pi\rho_m) + 0.08\cos(2\pi\rho_m) \tag{7}$$

where $\rho_m = (u_m^2 + v_m^2)^{1/2}/b_{\max}$ and $b_{\max}$ is the maximum baseline and effective aperture listed in Tables I and II. This window significantly reduces sidelobe levels at the cost of poorer angular resolution.

ΔS_m is the density taper weighting function and is equivalent to the differential area $dudv$ in an inverse Fourier transform operation. For regular grids, the sample density is constant, however, for the proposed grid as shown in Fig. 8, this must be computed for each visibility sample. For the proposed sampling pattern, ΔS_m is a product of two components, as follows:

$$\Delta S_m = \Delta S_{\text{ma}} \Delta S_{\text{mb}} \tag{8}$$

where ΔS_{ma} accounts for the polar distribution of the samples, and ΔS_{mb} accounts for the overlaps between these polar samples.

ΔS_{ma} is found as

$$\Delta S_{\text{ma}} = r_m \delta r \delta\theta \tag{9}$$

where r_m is the radial distance of the visibility samples to the centers of the circular samples, not the origin of the visibility, δr is the radial distance between successive visibility samples, and $\delta\theta$ is the angular distance between visibility samples.

Where these polar grids overlap, the weighting for these visibility samples must be divided by two

$$\Delta S_{\text{mb}} = \begin{cases} \frac{1}{2}, & \text{in overlap zone} \\ 1, & \text{otherwise.} \end{cases} \tag{10}$$

Density taper ΔS of the proposed array is shown in Fig. 8.

Using Blackman windowing, the normalized beam pattern, i.e., the array factor of the nine-companion Single-Element

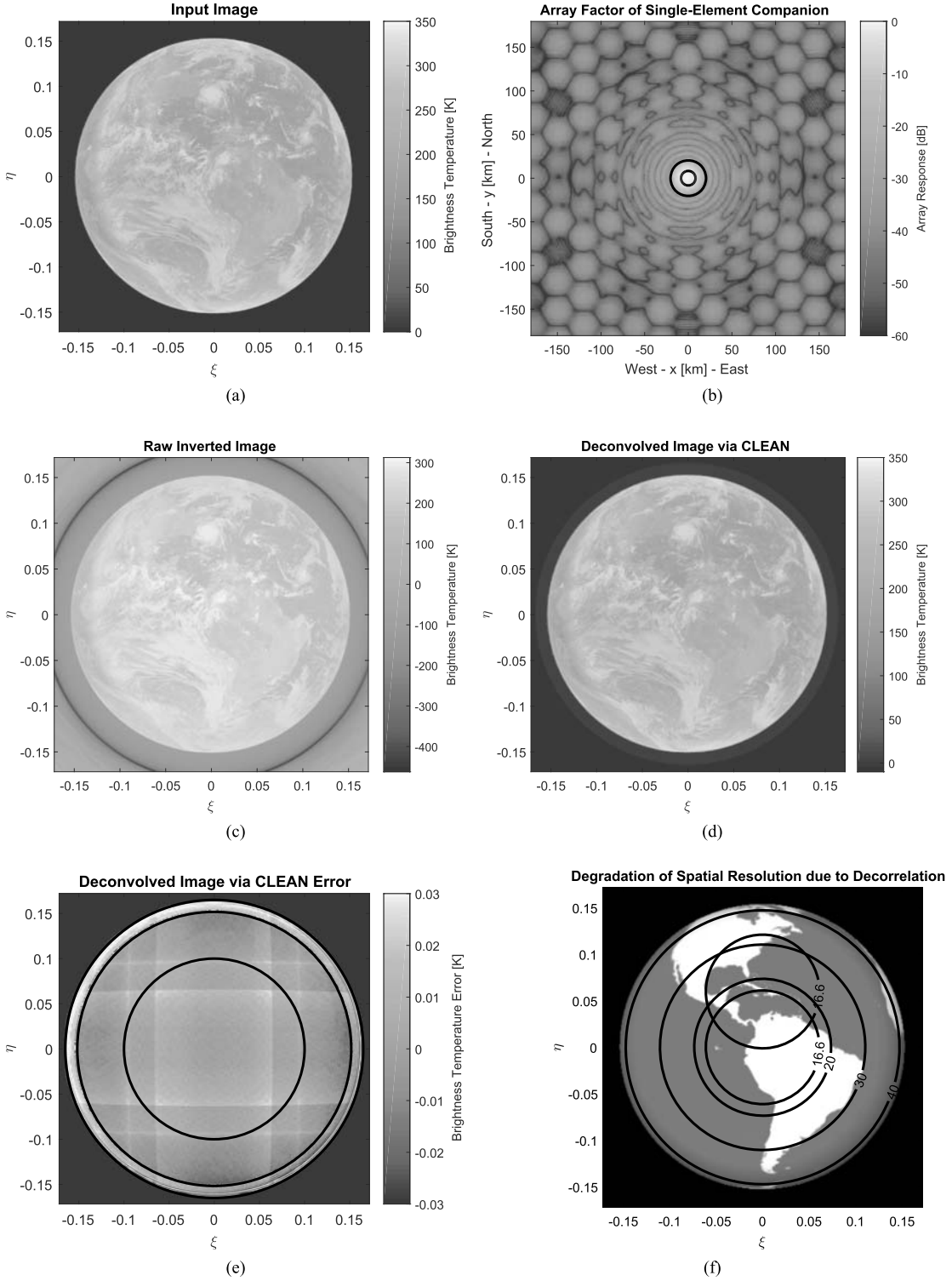

Fig. 9. (a) Input image of the Earth from geostationary Earth orbit. (b) Array Factor of nine-companion Single-Element Companion concept at 53 GHz as described in Table III. (b) Inner circle shows the half-power Beamwidth, and the outer circle shows the first Null. (c) Reconstructed map. (d) Output of the extended-CLEAN algorithm and (e) error of cleaned output, inner circle is where rms error is calculated. The location of Earth-sky horizon is at the second circle, and the interferometer field of view is the outer circle, within which the CLEAN operation is performed. (f) Contours of achievable spatial resolution (km) limited by decorrelation effects (Section V-B).

Companion concept is simulated at 53 GHz. The size of the array is summarized in Table III. The beam pattern is shown in Fig. 9(b), and the beam performance is shown in Table IV. The inner circle in Fig. 9(b) shows the full width at half-maximum beamwidth at 16.7 km diameter, and the outer circle shows the first null at 40.8 km diameter, both circular due to the circular windowing function. The hexagonal pattern of sidelobes is caused by the discontinuities defined in (10) at

TABLE III

SIMULATED PARAMETERS FOR THE SINGLE-ELEMENT COMPANION CONCEPT

Parameter	Value
Boom Length	4 m
Minimum Baseline	3λ
Number of Antennas per Arm	236
Number of Companions	9
Maximum Baseline	14.4 m
Windowing Function	Blackman

The beam produced by this array is shown in Fig. 9b.

TABLE IV

SIMULATED BEAM PERFORMANCE OF THE TWO CONSTELLATION CONCEPTS

	Concept 1	Concept 2
-3dB Beam Efficiency	7.2%	
Null Beam Efficiency	11.9%	
-3dB Full Beam Width	16.7 km	8.3 km
Null Full Beam Width	40.8 km	20.4 km
Side-Lobe Level	-29 dB	

For the 9-Companion Single-Element Companion (Concept 1) and the 6-satellite Array Duplicate (Concept 2) at 53 GHz from the geostationary orbit.

the boundaries between the overlapping regions, as well as the zeros present in (9), both of which have hexagonal symmetry. Given this beam, the CLEAN algorithm is applied to the raw reconstructed image to reduce brightness retrieval errors to an acceptable level [26], [27].

A. Performance of the Retrieval Algorithm

We now simulate the ideal performance of the arrays and find the quantization error of the retrieval algorithm. The nine-companion Single-Element Companion array is simulated without the presence of satellite relative position uncertainty and with infinite integration time. For the purposes of this paper, the test input image has been derived from GOES13 imagery data, rescaled in brightness such that brightness temperature is between 250 and 350 K, and cold sky brightness temperature is 2.73 K. While this test image, shown in Fig. 9(a), does not fully represent the brightness temperature map at 53 GHz, it does enable the verification of the interferometer spatial resolution. Following the procedure previously described, the array is simulated forward and back, producing the retrieved brightness temperature map.

The raw output is shown in Fig. 9(c) with a spatial resolution of 16.7 km at 53 GHz. Note the smearing at the horizon due to decorrelation, and the negative ring which marks the boundary to the first alias, beyond which the texture of the Earth alias is visible. Since the raw image is the input image convolved with the dirty beam, shown in Fig. 9(b), the CLEAN algorithm is used to deconvolve the raw image to reduce the error, as described in [26] and [27]. The array factor is used in conjunction with *a priori* knowledge (horizon location, and the average brightness temperature of the Earth and the cold sky) to iteratively clean the raw image until the rms of the residual within the alias-free field of view falls under a specified value. Note that the rotating arrays produce circular alias-free field of view. The result is then smoothed with a Blackman low-pass filter. The deconvolved result is shown in Fig. 9(d), with threshold residual of 0.001 K. Fig. 9(e) shows the retrieval error—the difference between the retrieved map and the weighted-average version of the input image T_B^f passed through a Blackman low-pass filter with equal interferometer beamwidth. The rms within the inner circle is 0.01 K, dominated by artifacts which are likely the result of operating within a circular field of view in a rectangular grid. This contribution is negligible compared to other expected sources of error.

The Array Duplicate concept produces an exactly identical visibility sampling pattern, and subsequently its beam is also identical to that of the Single-Element Companion concept, using the same inversion algorithm followed by the CLEAN process.

TABLE V

ERROR IN RETRIEVED BRIGHTNESS TEMPERATURE DUE TO SATELLITE RELATIVE POSITION UNCERTAINTY

Baseline uncertainty	Concept 1		Concept 2	
	In-plane	Three-axis	In-plane	Three-axis
Nominal	0.01 K		0.01 K	
0.01 λ	0.04 K	0.16 K	0.01 K	0.04 K
0.1 λ	0.09 K	1.17 K	0.04 K	0.44 K
1 λ	0.84 K	6.83 K	0.50 K	4.85 K
3.5 λ	/	0.016 K	/	0.016 K

Error for different uncertainty levels. Three-axis includes both in-plane and out-of-plane errors. The last row shows a case where satellites are dislocated by 3.5λ but their exact positions are known.

B. Effects of Satellite Relative Position Uncertainty

The visibility inversion process as described in (6) requires the correct knowledge of the baseline vectors (u, v, w), which are the relative separations between antenna phase centers. With free-flying antenna elements, this must be continuously measured, and uncertainties will be a major source of error in the retrieved brightness temperature map. This is now taken into account by simulating the array output with random errors in satellite relative position measurement of various magnitudes, assuming infinite integration time and arrays free of distortion, and attitude error. Errors of 0.01λ, 0.1λ and 1λ are included when simulating the array forward, and the map is retrieved using the error-free nominal baseline vectors, from which the retrieval error is found in the same manner as in Section IV-A.

Representative simulation results for the nine-companion Single-Element Companion concept (Concept 1) and the six-satellite Array Duplicate concept (Concept 2) are shown in Fig. 10. Since the result depends on the stochastic measurement errors, the simulation is run ten times and the average result is shown Table V. All outputs are processed by the CLEAN algorithm with 0.005 K as the threshold residual, which should allow us to reach the noise floor due to quantization. To allow direct comparison between the Single-Element Companion and the Array Duplicate concepts, the two concepts are simulated at equal spatial resolution of 16.7 km, by reducing the boom-length of the Array Duplicate option from 4 to 2 m.

It can be immediately seen that the out-of-plane errors have a larger impact than in-plane errors in both concepts,

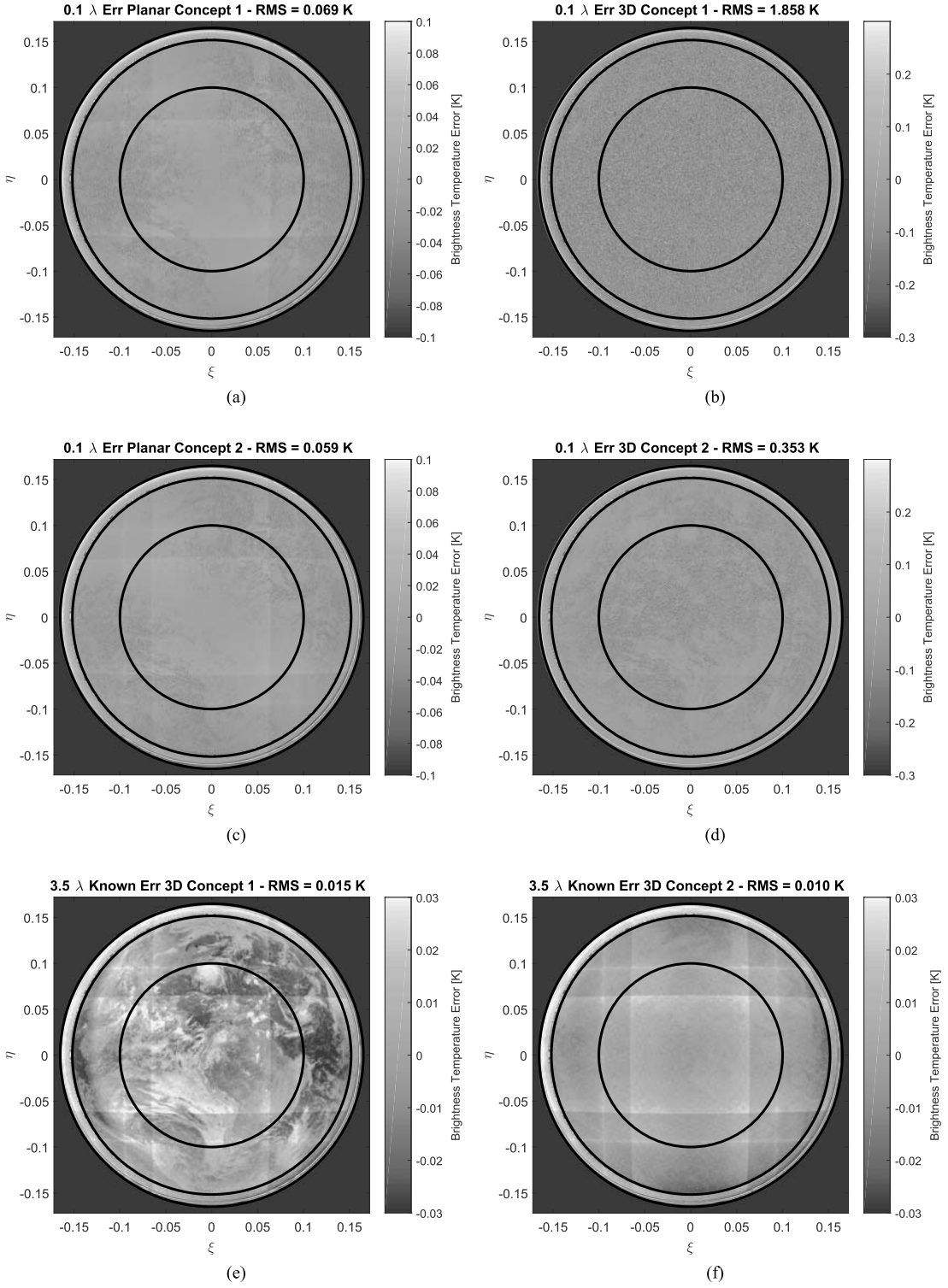

Fig. 10. Error map of the recovered brightness temperature due to 0.1λ random error in satellite relative position measurement. (a) In-plane and (b) three-axis for nine-companion Single-Element Companion concept. RMS is taken within the inner circle of radius 0.1. (c) In-plane and (d) three-axis error for six-satellite Array Duplicate concept. (e) and (f) Effect of 3.5λ dislocations that are exactly known. Summary of ten simulations shown in Table V.

showing that intersatellite ranging techniques must be sensitive to out-of-plane deviations. It can also be seen that the Array Duplicate concept is more robust against this type of baseline errors due to the presence of redundant intersatellite baselines. It is important to note that the cause of these errors is the uncertainties in the knowledge of the intersatellite relative positions, and not the presence of errors in the position itself. To demonstrate this, another simulation has been run where the

satellites are dislocated by 3.5λ, but their positions are exactly known. The resultant errors, shown in Fig. 10(e) and (f), are at the noise floor of the retrieval algorithm.

C. Radiometric Resolution

The expected radiometric resolutions of the two proposed concepts are now estimated by finding the expected variance in the output. The standard deviation of the retrieved brightness temperature map is given as follows [16]:

$$\Delta\hat{T}_B(\xi,\eta) = \frac{\Omega\sqrt{1-\xi^2-\eta^2}}{|F_n|^2} \cdot \sqrt{\sum_{m=1}^{N} \Delta S_m^2 W_m^2 \left(\sigma_{V_r}^2 + \sigma_{V_i}^2\right)} \quad (11)$$

for all nonredundant visibility samples, where σ_{V_r} and σ_{V_i} are the standard deviation of the real and imaginary components of the measured visibility samples, respectively. These are given as [28], [29]

$$\sigma_{V_r} = \sigma_{V_i} = \frac{(T_A + T_R)}{\sqrt{2B\tau/\eta_q}} \quad (12)$$

for integration time τ where T_A is the antenna temperature in response to the scene, which is found by solving (1) at the visibility origin. T_R is the receiver noise temperature at 250 K, and B is the predetection bandwidth at 400 MHz. Assuming 1-bit $\times$ 1-bit correlator at $2B$ frequency, η_q is 2.46. [28] Redundant visibility samples are averaged and, given the sufficient antenna separation, may be assumed uncorrelated. In this case, the variance of these measurements are reduced by the number of redundancies [28], [30].

Given the above, it is found that the three-element Single-Element Companion concept would require more than an hour to achieve 1 K resolution, whereas the three-satellite Array Duplicate concept requires 37 min. For larger arrays, the results are listed in Tables I and II. This result is mostly due to the absence of intersatellite baseline redundancy in the Single-Element Companion concept. The concept scales much more rapidly than the Array Duplicate, since the number of baselines scales linearly with the number of companions, rather than by the square as with the Array Duplicates. The rotating design of the interferometer also plays a major role, as it allows each visibility sample only a small fraction of the total integration time, which are 0.2% and 0.13% for the two concepts, respectively.

V. Discussion

A. Satellite Relative Position Tracking Requirements

The main result of this paper is the quantification of the required precision in the measurement of intersatellite relative position for formation flight interferometry. The consequences of measurement uncertainty have been simulated and summarized in Table V, and the results suggest that precision of a few percent of the wavelength is required for a viable interferometer. At the proposed 53-GHz center frequency, this corresponds to a few tens of micrometers, and this is required not only in ranging measurements, but in all three axes.

While this result is certainly challenging, it is just within reach of the current state of the art in intersatellite ranging and precision micro-Newton propulsion systems. In a separate study, the combination of GRAIL ranging instrument and the drag-free propulsion system on board LISA pathfinder has been simulated in a closed feedback loop to show that the combination can maintain a stable formation under geostationary orbital perturbation forces, and the resultant 3σ in the measured relative position is 64 μm [31].

As the interest in formation flying is rapidly growing, specifically designed future systems will materialize these figures. The upcoming Proba-3 mission will demonstrate 1σ measurement accuracy of 21 μm in the lateral direction and 30 μm in ranging at 150-m intersatellite separation [32]. Future formation flying telescope missions require 1–5 μm control accuracy in the lateral direction, and so far, 1σ of 150 μm has been demonstrated on ground at 300-m distance [33].

B. Decorrelation Effects

The proposed arrays face extreme decorrelation effects at the edge of field of view due to the very long baselines. For the nine-companion Single Element Companion concept, the maximum expected signal path delay is 8 ns with the nine-satellite Single-Element Companion concept, which means with 400-MHz bandwidth, the amplitude loss at the edge of field of view is $1-|\mathrm{sinc}(3.2)| = 95\%$. The loss in the visibility signal at the longest baselines is 6 dBK, which corresponds to the loss in SNR. The loss of spatial resolution in the radial direction is found as [25]

$$L = W\sqrt{\xi^2+\eta^2} = W\zeta. \quad (13)$$

At the edge of field of view ($\zeta = 0.172$), this is 42 km from the geostationary orbit, which is more than twice the interferometer's spatial resolution, listed in Tables I and II. The area in which the interferometer's spatial resolution is achievable is shown in Fig. 9(f).

This area can be increased by reducing the bandwidth or by "band-slicing" techniques [34]. However, both of these techniques are challenging as the sensitivity of the concepts are low, and the number of correlators required are already very large, as listed in Tables I and II. Slicing the bands would be impractical for the larger arrays as it would require 10 or more partitions.

An alternative approach is to introduce instrumental delays in order to move the center of spatial smearing to areas of higher importance, which can be modified during the mission. Fig. 9(f) also shows an area shifted to the northern hemisphere where the interferometer's spatial resolution is preserved.

C. Sensitivity and Integration Time

Due to the rotating design and minimal baseline redundancy, the radiometric resolution of both concepts is limited. The most sensitive configuration, as shown in Tables I and II, requires 37 min to resolve 1 K for 15-km spatial resolution. The Array Duplicate concept generally performs much better than the Single-Element Companion concept and suggests a relatively minor improvement would be sufficient, e.g.,

addition of antennas and pixel averaging. The Single-Element Companion concept, on the other hand, is especially sparse and a major innovation is necessary, or the rotating design may need to be replaced with a solid hexagonal central array. For applications where 1 K resolution is sufficient, methods for tracking the evolving atmosphere described in [35] may be directly applied for an immediate result.

VI. Conclusion

A novel interferometric radiometer concept using satellite formation flight has been presented, and this has been applied to geostationary atmospheric sounding at 53 GHz to show its practical implications. The concept introduces the capacity to synthesize apertures of conceptually unconstrained size in space for the first time. In addition to geostationary applications, such capability may be applied to achieve unprecedented spatial resolution at lower orbits, or to extend the accessible frequencies into lower frequency radio waves.

Two variants of the radiometer concept have been explored. The first is the Single-Element Companion concept with a rotating Y-shaped interferometer flying in formation with several companion microsatellites, achieving apertures of 14.4 m and larger. The second is the Array Duplicate concept with several identical satellites flying in formation, which can synthesize apertures of 28.8 m and larger. These aperture sizes represent twofold and fourfold improvement to the 7-m aperture synthesized by SMOS, and can be further increased by increasing the number of satellites.

The effect of uncertainties in the measured satellite relative position has been simulated and presented in Section IV-B. The arrays are found highly sensitive to this uncertainty, where errors as small as one tenth of the wavelength can result in up to 1.2 K error in the retrieved brightness temperature. This means micrometer-level intersatellite ranging is instrumental to the proposed concept at 53 GHz. The presence of redundant intersatellite baselines improves the array's robustness against this effect, where the Array Duplicate concept shows an error of 0.5 K rms at 0.1λ deviation.

While these requirements have already been met on ground-based demonstrations and will be soon on the Proba-3 mission, the more pressing challenge is in the interferometer's radiometric resolution. The Single-Element Companion concept is especially sparse and is not sensitive enough for atmospheric sounding in the current configuration. The Array Duplicate concept, on the other hand, is much more sensitive and the formation flight of three satellites requires 37 min for 1 K resolution. The challenge then is in implementing the large number of correlators in the order of 10^6-10^7 antenna pairs.

Acknowledgment

All data supporting this paper are openly available from the University of Southampton repository at http://doi.org/10.5258/SOTON/D0398.

References

[1] J. Font *et al.*, "SMOS: The challenging sea surface salinity measurement from space," *Proc. IEEE*, vol. 98, no. 5, pp. 649–665, May 2010.

[2] A. Hou *et al.*, "The global precipitation measurement mission," *Bull. Amer. Meteorol. Soc.*, vol. 95, no. 1, pp. 701–722, May 2014.

[3] U. Klein, C.-C. Lin, N. Atkinson, J. Charlton, and C. Philpot, "Future microwave radiometers in geostationary and medium earth orbit," in *Proc. IEEE Int. Geosci. Remote Sens. Symp. (IGARSS)*, Jul. 2003, pp. 2158–2160.

[4] B. Lambrigtsen, T. Gaier, P. Kangaslahti, B. Lim, A. Tanner, and C. Ruf, "Enabling the NASA decadal-survey 'PATH' mission," in *Proc. IEEE Int. Geosci. Remote Sens. Symp. (IGARSS)*, Beijing, China, Jul. 2016, pp. 3949–3951.

[5] J. Christensen *et al.*, "GAS: The geostationary atmospheric sounder," in *Proc. IEEE Geosci. Remote Sens. Symp. (IGARSS)*, Jul. 2007, pp. 223–226.

[6] H. Liu *et al.*, "The geostationary interferometric microwave sounder (GIMS): Instrument overview and recent progress," in *Proc. IEEE Geosci. Remote Sens. Symp. (IGARSS)*, Jul. 2011, pp. 3629–3632.

[7] A. K. Sugihara El Maghraby, A. Grubišić, C. Colombo, and A. Tatnall, "A novel approach to microwave interferometric radiometry in the geostationary orbit using formation flight," in *Proc. IAC 67th Int. Astron. Congr.*, Guadalajara, Mexico, 2016. [Online]. Available: http://iafastro.directory/iac/archive/browse/IAC-16/B1/2/33950/

[8] W. Zheng, H. Hsu, M. Zhong, and M. Yun, "Precise recovery of the Earth's gravitational field with GRACE: Intersatellite range-rate interpolation approach," *IEEE Geosci. Remote Sens. Lett.*, vol. 9, no. 3, pp. 422–426, May 2012.

[9] D. G. Enzer, R. T. Wang, and W. M. Klipstein, "GRAIL—A microwave ranging instrument to map out the lunar gravity field," in *Proc. IEEE Int. Freq. Control Symp.*, Newport Beach, CA, USA, Jun. 2010, pp. 572–577.

[10] M. Stephens *et al.*, "Demonstration of an interferometric laser ranging system for a follow-on gravity mission to GRACE," in *Proc. IEEE Int. Symp. Geosci. Remote Sens.*, Denver, CO, USA, Aug. 2006, pp. 1115–1118.

[11] G. Krieger *et al.*, "TanDEM-X: A satellite formation for high-resolution SAR interferometry," in *Proc. IET Int. Conf. Radar Syst.*, Edinburgh, U.K., 2007, pp. 1–5.

[12] K. Danzmann *et al.*, "LISA—Laser interferometer space antenna: A proposal in response to the ESA call for L3 mission concepts," Albert Einstein Inst. Hanover, Leibniz Univ. Hanover, Max Planck Inst. Gravitational Phys., Hannover, Germany, Tech. Rep., 2017.

[13] S. Bandyopadhyay, G. P. Subramanian, R. Foust, D. Morgan, S.-J. Chung, and F. Hadaegh, "A review of impending small satellite formation flying missions," in *Proc. 53rd AIAA Aerosp. Sci. Meeting*, 2015, p. 1623.

[14] I. Corbella, N. Duffo, M. Vall-llossera, A. Camps, and F. Torres, "The visibility function in interferometric aperture synthesis radiometry," *IEEE Trans. Geosci. Remote Sens.*, vol. 42, no. 8, pp. 1677–1682, Aug. 2004.

[15] A. Camps, I. Corbella, F. Torres, M. Vall-Llossera, and N. Duffo, "Polarimetric formulation of the visibility function equation including cross-polar antenna patterns," *IEEE Geosci. Remote Sens. Lett.*, vol. 2, no. 3, pp. 292–295, Jul. 2005.

[16] A. B. Tanner *et al.*, "Initial results of the geostationary synthetic thinned array radiometer (GeoSTAR) demonstrator instrument," *IEEE Trans. Geosci. Remote Sens.*, vol. 45, no. 7, pp. 1947–1957, Jul. 2007.

[17] A. Camps, J. Bará, I. C. Sanahuja, and F. Torres, "The processing of hexagonally sampled signals with standard rectangular techniques: Application to 2-D large aperture synthesis interferometric radiometers," *IEEE Trans. Geosci. Remote Sens.*, vol. 35, no. 1, pp. 183–190, Jan. 1997.

[18] I. Corbella, M. Martin-Neira, R. Oliva, F. Torres, and N. Duffo, "Reduction of secondary lobes in aperture synthesis radiometry," *IEEE Geosci. Remote Sens. Lett.*, vol. 9, no. 5, pp. 977–979, Sep. 2012.

[19] J. Bará, A. Camps, F. Torres, and I. Corbella, "Angular resolution of two-dimensional, hexagonally sampled interferometric radiometers," *Radio Sci.*, vol. 33, no. 5, pp. 1459–1473, Sep./Oct. 1998.

[20] F. Torres, A. B. Tanner, S. T. Brown, and B. H. Lambrigsten, "Analysis of array distortion in a microwave interferometric radiometer: Application to the GeoSTAR project," *IEEE Trans. Geosci. Remote Sens.*, vol. 45, no. 7, pp. 1958–1966, Jul. 2007.

[21] X. Zhou, H. Sun, J. He, and X. Lu, "NUFFT-based iterative reconstruction algorithm for synthetic aperture imaging radiometers," *IEEE Geosci. Remote Sens. Lett.*, vol. 6, no. 2, pp. 273–276, Apr. 2009.

[22] J. A. Fessler and B. P. Sutton, "Nonuniform fast Fourier transforms using min-max interpolation," *IEEE Trans. Signal Process.*, vol. 51, no. 2, pp. 560–574, Feb. 2003.

[23] C. Zhang, J. Wu, and W. Sun, "Applications of Pseudo-polar FFT in synthetic aperture radiometer imaging," *PIERS Online*, vol. 3, no. 1, pp. 25–30, 2007.
[24] A. Averbuch, R. R. Coifman, D. L. Donoho, M. Elad, and M. Israeli, "Fast and accurate polar Fourier transform," *Appl. Comput. Harmon. Anal.*, vol. 21, no. 2, pp. 145–167, 2006.
[25] A. Camps, "Application of interferometric radiometry to Earth observation," Ph.D. dissertation, Dept. Signal Theory Commun., Polytechnic Univ. Catalonia, Barcelona, Spain, 1996.
[26] A. Camps, J. Bará, F. Torres, and I. Corbella, "Extension of the clean technique to the microwave imaging of continuous thermal sources by means of aperture synthesis radiometers," *Prog. Electromagn. Res.*, vol. 18, pp. 67–83, 1998. [Online]. Available: http://www.jpier.org/PIER/pier.php?volume=18
[27] A. Camps *et al.*, "Microwave imaging radiometers by aperture synthesis performance simulator (Part 2): Instrument modeling, calibration, and image reconstruction algorithms," *J. Imag.*, vol. 2, no. 2, p. 18, 2016.
[28] A. Camps, I. Corbella, J. Bará, and F. Torres, "Radiometric sensitivity computation in aperture synthesis interferometric radiometry," *IEEE Trans. Geosci. Remote Sens.*, vol. 36, no. 2, pp. 680–685, Mar. 1998.
[29] C. S. Ruf, C. T. Swift, A. B. Tanner, and D. M. Le Vine, "Interferometric synthetic aperture microwave radiometry for the remote sensing of the Earth," *IEEE Trans. Geosci. Remote Sens.*, vol. GRS-26, no. 5, pp. 597–611, Sep. 1988.
[30] J. Bará, A. Camps, F. Torres, and I. Corbella, "The correlation of visibility noise and its impact on the radiometric resolution of an aperture synthesis radiometer," *IEEE Trans. Geosci. Remote Sens.*, vol. 38, no. 5, pp. 2423–2426, Sep. 2000.
[31] A. K. Sugihara El Maghraby, A. Grubišić, C. Colombo, and A. Tatnall, "A constellation concept for microwave interferometric radiometry from geostationary orbit: Sensor and actuator requirements for formation control," in *Proc. 9th Int. Workshop Satellite Constellations Formation Flying*, Jun. 2017.
[32] L. T. Castellani *et al.*, "PROBA-3 mission," *Int. J. Space Sci. Eng.*, vol. 1, no. 4, pp. 349–366, 2013.
[33] A.-M. Novo-Gradac, G. Yang, S. Li, and J. M. Davila, "Relative position snsing for a precision formation flying space telescope," in *Proc. 9th Int. Workshop Satellite Constellations Formation Flying*, Boulder, Colorado, Jun. 2017.
[34] M. A. Fischman and A. W. England, "A technique for reducing fringe washing effects in L-band aperture synthesis radiometry," in *Proc. IEEE Int. Geosci. Remote Sens. Symp. (IGARSS)*, vol. 7. Honolulu, HI, USA, Jul. 2000, pp. 3154–3156.
[35] Y. Zhang, H. Liu, J. Wu, C. Zhang, and J. He, "Method to reduce imaging errors in dynamic target observation of the geostationary interferometric microwave sounder," *IEEE Geosci. Remote Sens. Lett.*, vol. 14, no. 2, pp. 267–271, Feb. 2017.

Ahmed Kiyoshi Sugihara El Maghraby received the M.Eng. degree in space systems engineering from the University of Southampton, Southampton, U.K., in 2014, where he is currently pursuing the Ph.D. degree with the Astronautics Research Group.

He was involved in an extremely low altitude satellite photogrammetry mission concept. His research interests include applying satellite formation flight to passive microwave interferometry, with particular interest in applying this to geostationary microwave radiometry for real-time observation of meteorological phenomena.

Angelo Grubišić was born in Walsall, U.K., in 1981. He received the M.Sc. degree from the International Space University, Illkirch-Graffenstaden, France, in 2005, and the Ph.D. degree from the University of Southampton, Southampton, U.K., in 2009.

He was involved in the development and testing of gridded ion thrusters and other electric propulsion systems, including the NSTAR ion thruster at NASA JPL and the T6 ion thruster for QinetiQ. From 2010 to 2013, he was responsible for designing and leading the systems level coupling and qualification tests for the Bepi Colombo electric propulsion system on the Mercury Transfer Module, the highest power dual ion thruster system to date. Since 2013, he has been pioneering selective laser melting additive manufacturing technologies for production of advanced propulsion systems as a Lecturer with the Astronautics Group, University of Southampton.

Camilla Colombo received the M.Eng. degree in aerospace engineering from the Politecnico di Milano, Milan, Italy, in 2005, and the Ph.D. degree from the University of Glasgow, Glasgow, U.K., in 2010.

She is currently an Associate Professor with the Politecnico di Milano, where she leads a European Research Council Starting Grant on the project COMPASS Control for Orbit Maneuvering through Perturbations for Application to Space Systems. Her work spans orbital dynamics, space debris, high area-to-mass spacecraft, trajectory design and control, and asteroid deflection. She is involved in the EC Funded Project ReDSHIFT and contracts funded by the European Space Agency (ESA). From 2012 to 2016, she was with the University of Southampton, Southampton, U.K., where she was a Lecturer of spacecraft system engineering courses run at ESA and lead research work on space debris and libration orbit missions. In 2013, she was a Research Fellow with the Politecnico di Milano, sponsored by a Marie Curie Fellowship. She was a Research Fellow with the University of Strathclyde, Glasgow, and a Research Associate with the University of Glasgow. She has authored or co-authored 35 journal papers and 100 conference publications

Dr. Colombo was a recipient of the William Wilson Scott Award Scholarship in 2009 for her Ph.D. thesis on Optimal Trajectory Design for Interception and Deflection of Near Earth Objects.

Adrian Tatnall received the B.Sc. degree in physics from Exeter University, Exeter, U.K., in 1973, and the Ph.D. degree from Sheffield University, Sheffield, U.K., in 1978.

He was a Post-Doctoral Research Assistant with York University, York, U.K., and a Senior Space Systems Engineer with British Aerospace, Farnborough. In 1988, he joined the Department of Aeronautics and Astronautics, University of Southampton, Southampton, U.K., and became the Head of the Astronautics Group, University of Southampton, and a Senior Tutor at the University of Southampton. He was an Organizer and a Lecturer of spacecraft system engineering courses run for industry at the European Space Agency and Southampton for 25 years. He has authored chapters on systems engineering and telecommunications in the book *Space Systems Engineering* edited by Fortescue, Stark, and Swinerd. His research interests include internal waves, ocean color, SAR, formation flying, neural nets, especially, in the design and modeling of the performance of satellite passive microwave instruments.

Dr. Tatnall served on the Space Committee of the U.K. Royal Aeronautical Society for many years.